

Journal of Geophysical Research: Solid Earth

RESEARCH ARTICLE

10.1029/2017JB015240

Key Points:

- We observe frequent air traffic events in continuous seismic waveforms recorded by a tight array on the San Jacinto fault zone
- Time-frequency analysis shows clear Doppler effects that can be modeled with basic equations and fitted well with reasonable parameters
- The daily duration of air traffic events is likely to exceed in many places the total time covered by earthquakes

Supporting Information:

- Supporting Information S1
- Data Set S1
- Data Set S2

Correspondence to:

H. Meng,
haoranme@usc.edu

Citation:

Meng, H., & Ben-Zion, Y. (2018). Characteristics of airplanes and helicopters recorded by a dense seismic array near Anza California. *Journal of Geophysical Research: Solid Earth*, 123. <https://doi.org/10.1029/2017JB015240>

Received 16 NOV 2017

Accepted 2 MAY 2018

Accepted article online 11 MAY 2018

Characteristics of Airplanes and Helicopters Recorded by a Dense Seismic Array Near Anza California

Haoran Meng¹  and Yehuda Ben-Zion¹ 

¹Department of Earth Sciences, University of Southern California, Los Angeles, CA, USA

Abstract We observe frequent air traffic events in continuous seismic waveforms recorded for about 30 days by 1,108 vertical geophones in a tight array on the San Jacinto fault zone. The waveforms of the air traffic events resemble tremor or collections of small earthquakes. However, time-frequency analysis reveals clear Doppler effects that can be modeled with basic equations and fitted well with parameters corresponding to airplanes and helicopters. The flying traces can be inverted by fitting the parameters at each station across the entire array. About 31 air traffic events are detected per day in the relatively remote study area, with peak activity from about 8:00 to 18:00 and significantly fewer events between 23:00 and 4:00 local time. The average event duration is about 200 s, so they cover together >7% of the day. To estimate the total time covered by earthquakes, we derive a scaling relation $\log_{10}(M) = 0.41M + 0.89$ between earthquake duration and magnitudes using data of 266 earthquakes in the magnitude range $0 \leq M \leq 3$. The results indicate that in most places, the duration of air traffic events is likely to exceed considerably the total time covered by earthquakes.

1. Introduction

The growing quantity and quality of continuous waveforms recorded by seismic networks and temporary arrays at various scales, coupled with improved sensors and processing techniques, provide increasing opportunities for detection and analyses of weak sources of ground motion. Detection and analyses of events with signal-to-noise (SNR) ratios below 1 is now commonly done in studies of earthquakes, tremor, and induced seismicity around the world (e.g., Chen et al., 2017; Ross et al., 2017; Shelly et al., 2007; Zigone et al., 2012). The association of weak signals with $\text{SNR} \leq 1$ with genuine seismic sources below the surface (earthquakes and tremor) requires detailed understanding of the differences between such events and sources of energy at and above the surface. These include various types of cultural noise at the surface (e.g., cars and trains), interactions of the wind with surface structures, and sources in the atmosphere (e.g., storms and air traffic).

In addition to developing reliable catalogs of weak subsurface seismic events, the ability to detect and classify different sources that produce small episodic ground motion is important for tomographic imaging based on the ambient seismic noise. These studies, which are now done routinely in many environments (e.g., Campillo et al., 2011; Nakata et al., 2015), require a diffuse wavefield (e.g., Shapiro et al., 2000; Weaver, 1982) and removal from observed waveforms of all other sources (e.g., Bensen et al., 2007). More generally, detailed characterization of different types of common sources of ground motion contributes to a more complete understanding of the observed seismic waveforms.

In the present work we quantify characteristics of airplane and helicopter signals recorded by a dense seismic array with 1,108 vertical ZLand geophones (10 Hz) centered on the Clark branch of the San Jacinto fault zone (SJFZ) at the Sage Brush Flat (SGB) site southeast of Anza, California (red box Figure 1a). The array recorded continuously at 500 Hz from 7 May 2014 to 13 June 2014 and covered an area of about 600 m × 600 m (Figure 1c) with nominal sensor spacing of 10 m normal to the fault and 30 m along strike (Ben-Zion et al., 2015). The array data have been used for detailed imaging of the fault zone structure based on the ambient seismic noise (Hillers et al., 2016; Roux et al., 2016) and detection of microearthquakes (Gradon et al., 2017; Meng & Ben-Zion, 2018). The focus in the present work on air traffic events is complementary to these studies. In addition to data of the dense ZLand array, we examine waveforms recorded by a borehole seismometer ~150 m deep at station B946 (green triangle in Figure 1c), and use data of a strong ground motion station SGBFO (yellow triangle in Figure 1c) to measure durations of cataloged earthquakes in year 2014. As a control test, we also analyze data of a broadband station JFS4 at the Jackass Flat site (red triangle in Figure 1a) with

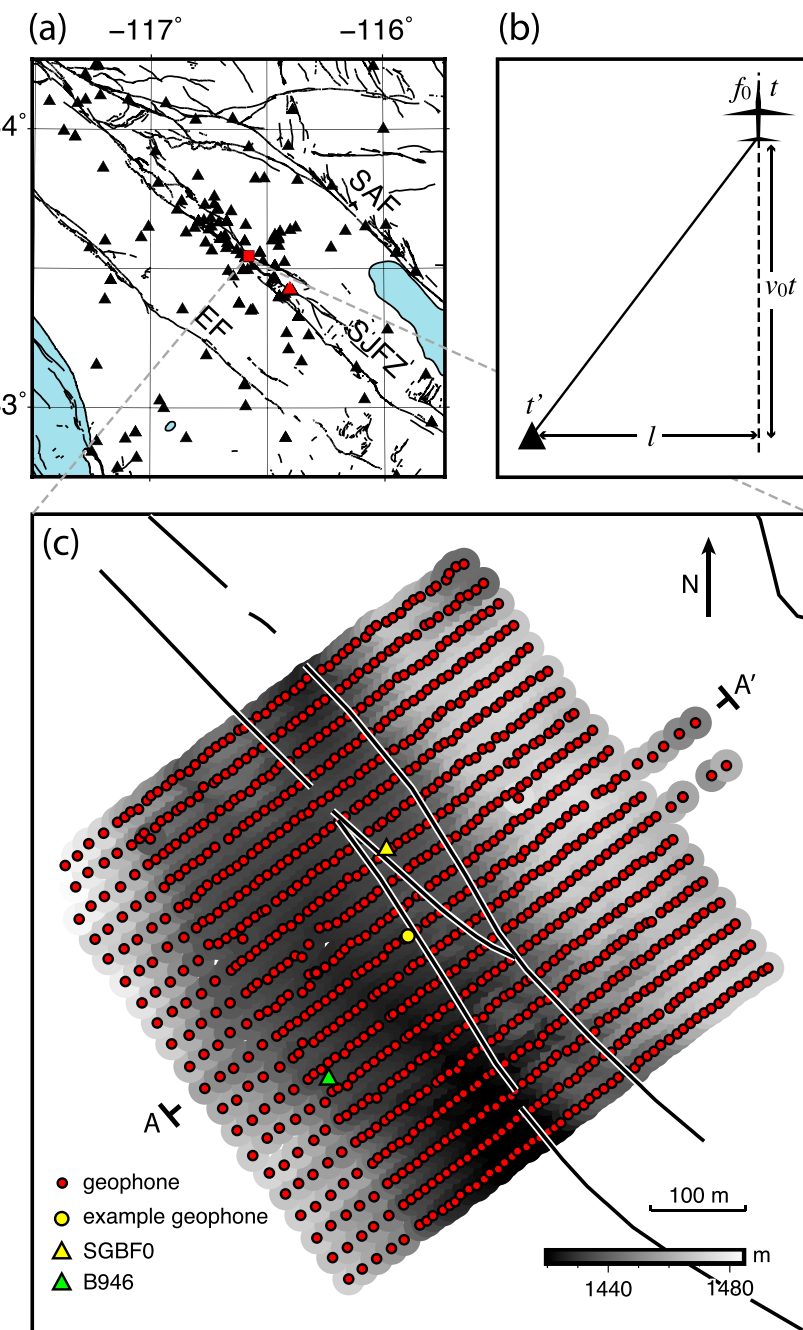


Figure 1. (a) A regional map showing the dense array on the San Jacinto fault zone (red square), regional seismic stations (black triangles) and station JFS4 (red triangle). (b) A conceptual diagram of an airplane flying over a station (black triangle). (c) Zoom in view of the dense deployment at the Sage Brush Flat (SGB) site. The red circles denote vertical component geophones, the yellow circle marks a geophone used to present example data, the yellow triangle denotes strong ground motion station SGBF0, and the green triangle marks 148-m-deep borehole station B946. Data recorded by the instruments along profile A-A' are shown in Figure 6. The background gray colors represent topography and the lines show surface traces of the Clark fault at the site.

known record of a helicopter flying nearby. The borehole sensor at B946 records continuously at 100 Hz, and the sensors at SGBF0 and JFS4 record continuously at 200 Hz.

In the next section we present and analyze example observations of airplane and helicopter events that generate wave trains with typical duration of several minutes. The appearance of these events in waveforms resembles in casual analysis tremor or a sequence of small earthquakes, but they have clear Doppler

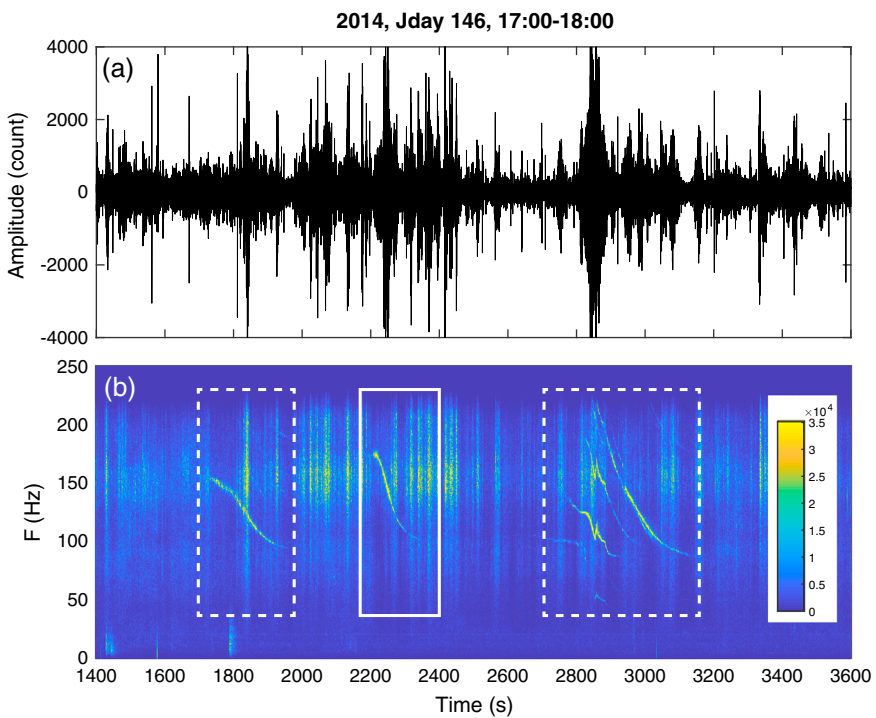


Figure 2. (a) A raw waveform recorded by the marked geophone in Figure 1c of the dense deployment during Julian day 146 (2014), 17:23:20 to 18:00:00 GMT. (b) corresponding spectrogram with solid and dashed white boxes marking air traffic events.

effects that can be easily recognized with time-frequency analysis and modeled with basic analytical expressions. The air traffic events cover in the study area >7% of the total time in a day, so they make a significant contribution to the observed ground motion. In large cities with highly active airports such as Los Angeles, the air traffic events can cover >75% of the day. Two appendices provide material on estimating the flying traces from seismic array data and a scaling relation between earthquake durations and magnitudes. The results are discussed and summarized in section 3 of the paper.

2. Analysis

2.1. Observations

We start the analysis by examining raw waveforms recorded by the dense array and corresponding spectrograms. Figure 2a shows example results from a 2,200-s time window in Julian day 146, 2014, recorded by the sensor marked in Figure 1c. The raw waveforms in this and other examples include frequent tremor-like wave trains with significant amplitude over durations that are hundreds of seconds long (Figures 2–7 and S1–S4 in the supporting information). To obtain spectrograms, the waveforms are transformed to the frequency domain using short moving time intervals of 1,024 samples with 512 overlapping samples. The results reveal clear characteristic signals that start with relatively high frequency and drop to low frequency smoothly with relatively flat portions at the high- and low-frequency ends (e.g., yellow curve in Figure 3b). Using different short time windows (e.g., 512 or 2,048 samples) and overlap settings (e.g., 256 or 2,014 samples) give essentially the same results. Converting the waveform in Figure 3a (associated with the white solid box in Figure 2b) into an audio signal produces a sound that includes a signal resembling the Doppler effect of an aircraft flying over (supporting information Audio S1).

We observe many such signals with clear Doppler effects and frequencies that usually decrease with time. This has a simple interpretation in terms of radiation from moving sources. One type of these signals has only one overtone, as the yellow curve in the spectrogram in Figure 3b, which generally spans a frequency range above 70 Hz. Another type of signals has multiple overtones in the spectrogram and spans a frequency range above 15 Hz (Figure 5b). More complex signals that appear to be distorted versions of the above two

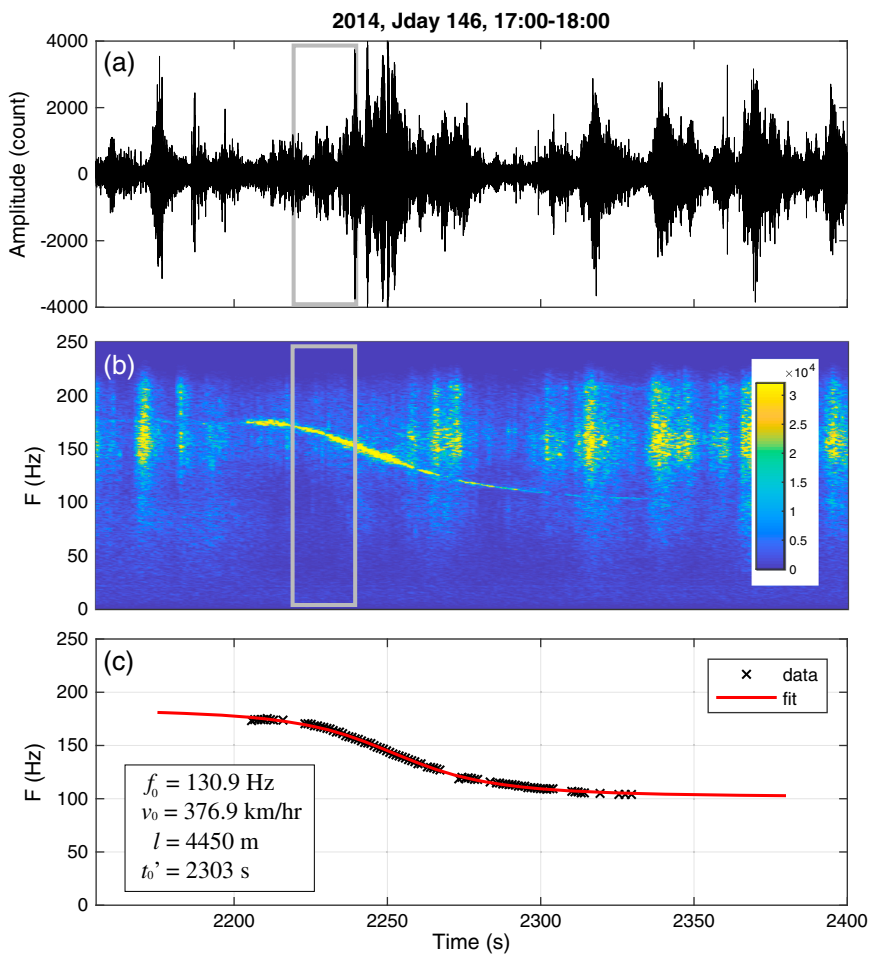


Figure 3. (a) Zoom in waveform for an airplane event in the white solid box in Figure 2 recorded by the example station in Figure 1. (b) A corresponding spectrogram. The gray boxes denote 20-s window of data shown by Figure 6a. (c) Time and frequency data (black crosses) picked in the spectrogram in (b) and line fit to the data based on equation (1) (red curve). The inferred parameters for the airplane are indicated in the box.

types (e.g., the right white dashed box in Figure 2b) occur much less frequently. All these signals have significantly larger amplitudes than the background noise and they last for minutes.

Figure 6a displays 20-s raw waveforms of the event in Figure 3 recorded by the geophones indicated by profile AA' in Figure 1c. Figure 6b displays corresponding waveforms associated with a local earthquake with magnitude $M_L = 0.5$ and hypocentral distance of about 12 km. The apparent velocity of the coherent phase in Figure 6a is $\sim 300 \text{ m/s}$, while the apparent velocity of coherent phases in Figure 6b is much higher. The slow apparent velocity of the air traffic signal and surface locations of the geophones indicate propagation that is primarily in the air. However, the velocity of high-frequency Rayleigh waves at the site is $\sim 300\text{--}400 \text{ m/s}$ (Hillers et al., 2016; Meng & Ben-Zion, 2018; Roux et al., 2016), so there are likely also induced signals that propagate in the subsurface material. Figure S1 shows waveforms and spectrograms generated by the helicopter event in Figure 5 and recorded by a 148 m deep sensor in borehole station B946. These results indicate that the acoustic signal can indeed produce coupled vibrations in the ground. However, the borehole signals are relatively weak compared to the signals recorded at the surface because of strong attenuation of the shallow material and possible weak coupling of the acoustic waves to the ground.

2.2. Modeling

Time-frequency analysis and basic analytical results show that the discussed signals have clear changing-frequency signatures that can be modeled as Doppler effects associated with airplanes or helicopters

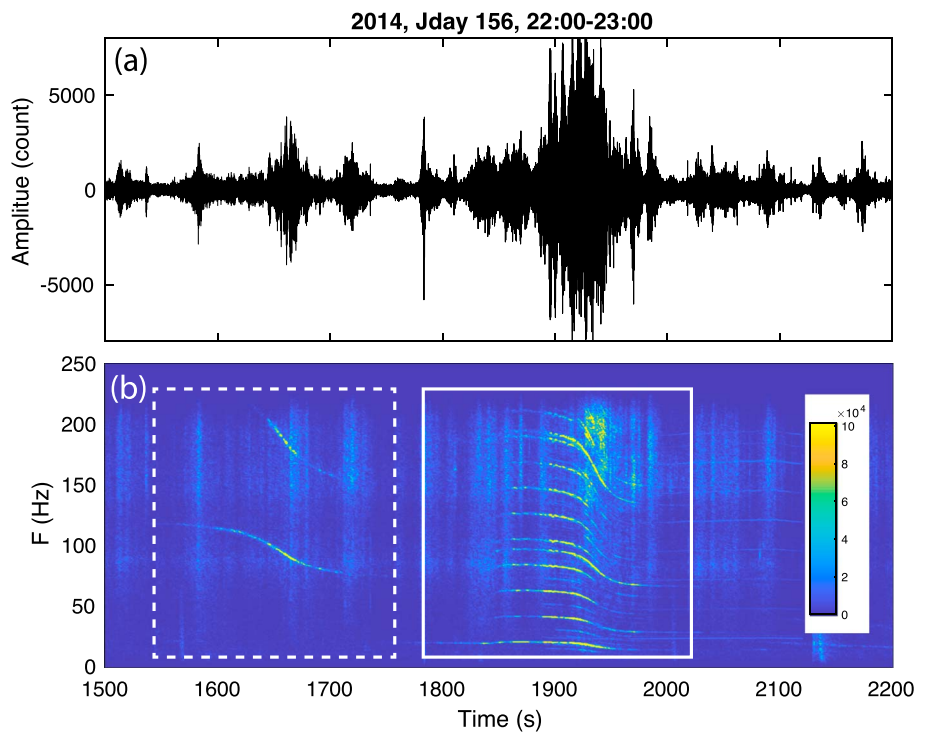


Figure 4. (a) A raw waveform of the marked geophone in Figure 1c for Julian day 156, 22:25:00 to 22:36:40 GMT. (b) A corresponding spectrogram with solid and dashed white boxes marking air traffic events.

flying nearby. To analyze quantitatively the signals highlighted by the solid white box in Figure 2b, we consider a simple model with an aircraft flying with constant velocity along a straight path (Figure 1b). The aircraft is assumed to be sufficiently far from the seismic stations to be represented by a point source radiating acoustic waves centered on frequency f_0 . The signal frequency recorded by a seismic station at the surface is

$$f(t') = f_0 \frac{1}{1 + \frac{v_0}{c} \frac{v_0 t}{\sqrt{l^2 + (v_0 t)^2}}}, \quad (1)$$

where v_0 is the aircraft velocity, l is the shortest distance between the station and the aircraft path, t is time, and c is the acoustic wave propagation velocity (~ 343 m/s). A wave generated by the aircraft at time t arrives at the station at time t'

$$t' = t + \frac{\sqrt{l^2 + (v_0 t)^2}}{c}. \quad (2)$$

Solving equation (2) and keeping the causal solution with $t' > t$ gives

$$t = \frac{t' - \sqrt{t'^2 - \left(1 - \frac{v_0^2}{c^2}\right)\left(t'^2 - \frac{l^2}{c^2}\right)}}{1 - \frac{v_0^2}{c^2}}. \quad (3a)$$

To model data with arbitrary reference time, we add a reference t_0' value to equation (3a)

$$t = \frac{(t' - t_0') - \sqrt{(t' - t_0')^2 - \left(1 - \frac{v_0^2}{c^2}\right)\left[(t' - t_0')^2 - \frac{l^2}{c^2}\right]}}{1 - \frac{v_0^2}{c^2}}. \quad (3b)$$

The above expressions have only four unknown parameters that can be easily determined from the observed data.

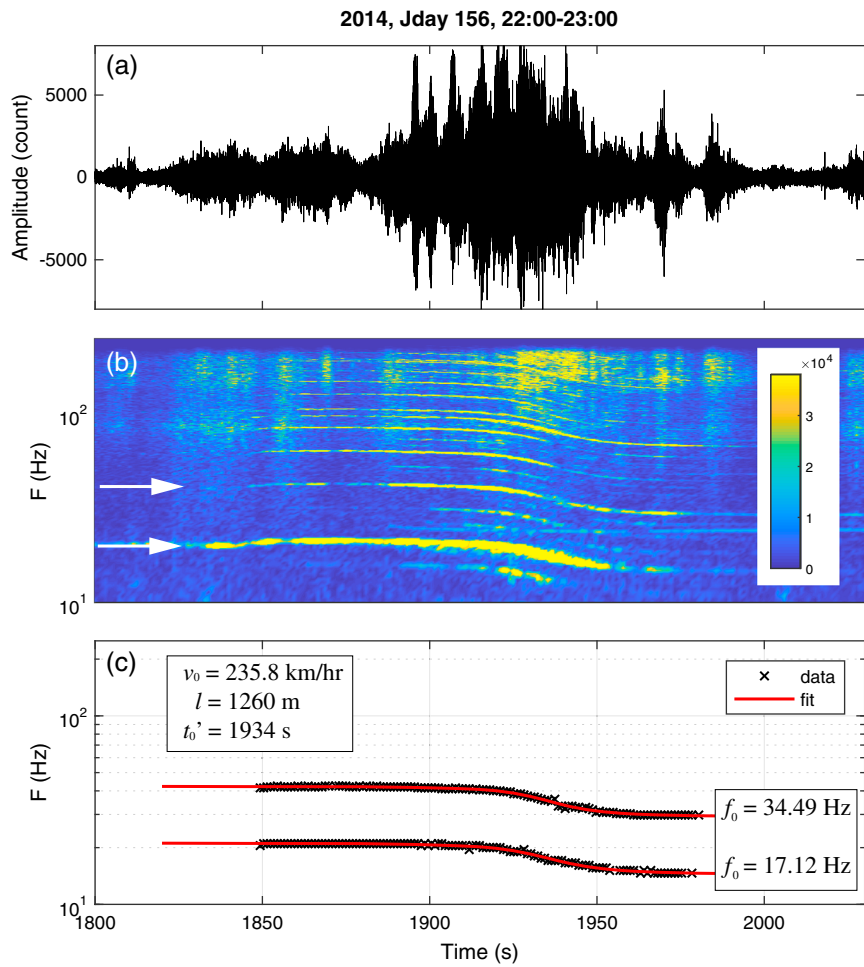


Figure 5. (a) Zoom in waveform for a helicopter event in the white solid box in Figure 4 recorded by the marked station in Figure 1c. (b) A corresponding spectrogram with vertical axis in log scale. The white arrows in (b) and (c) denote the two strong overtones picked for analysis. (c) Time and frequency data (black crosses) for two overtones picked in the spectrogram in (b) and line fit to the data based on equation (1) (red curves). The inferred parameters for the helicopter are indicated in the boxes.

For a given group of parameters $m_0 = [f_0 \ v_0 \ l \ t_0']^T$, the frequency at a receiver $f(t') = f(m_0; t')$ is predicted by equations (1) and (3b). Starting from a reasonable initial model m_0 and observed frequency $f_{\text{ob}}(t')$, the final model m is inverted by improving the data fit iteratively using

$$m = m_0 + (G^T G)^{-1} G^T [f_{\text{ob}}(t') - f(m_0; t')], \quad (4a)$$

$$G = \left. \frac{\partial f}{\partial m} \right|_{m=m_0}. \quad (4b)$$

Taking as example the data shown in Figures 3a and 3b, we extract the time and frequency signals of the yellow curve in Figure 3b by finding the frequencies of peak amplitudes for all times slices in the spectrogram. The black crosses in Figure 3c denote the picked time and frequency data. Outliers with large misfits are removed iteratively in the inversion for the Doppler parameters. The red curve in Figure 3c is obtained by inserting equation (1) into (3b), and it fits the observed values very well. The fitting parameters (frequency $f_0 \sim 131 \text{ Hz}$, velocity $v_0 \sim 377 \text{ km/hr}$, distance $l \sim 4.5 \text{ km}$, and $t_0' \sim 2,303 \text{ s}$) have reasonable values for a small airplane or a passenger airplane that is climbing to (or descending from) a cruising altitude. Processing the waveforms at the remaining stations indicates a clear trend of l and t_0' across the entire array (Figures A2a and A2b). This is used to determine the flying trace by the technique discussed in Appendix A.

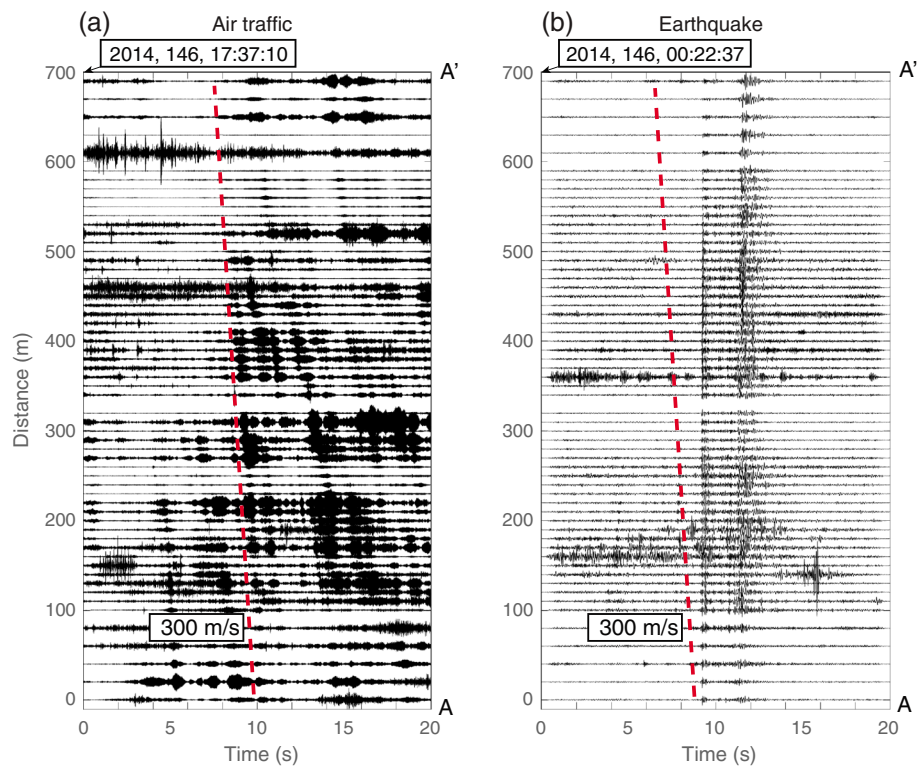


Figure 6. (a) Raw 20-s waveforms of air traffic event in Figure 3 recorded by geophones in profile AA' of Figure 1c. (b) Corresponding 20-s waveforms of a local seismic event (band-pass filtered from 1 to 20 Hz). The red dashed lines denote apparent slowness of 300 m/s.

Another type of air traffic event is represented by the example in the white solid box of Figure 4b. The source of this event is an aircraft with multifrequency radiation. Zooming on the corresponding time window 1,800–2,030 s, the spectrogram is displayed in Figure 5b with a log scale for the frequency. Taking the logarithm on both sides of equation (1), we have

$$\log f(t') = \log f_0 - \log \left(1 + \frac{v_0}{c} \frac{v_0 t}{\sqrt{t^2 + (v_0 t)^2}} \right). \quad (5)$$

Equation (5) shows that multiple overtones with different f_0 values in the same aircraft, moving with same velocity, distance, and reference time, have identical second term on the right side (associated with time). This implies that characteristics associated with different f_0 values radiated from the same moving object are shifted up or down on spectrograms using log scale for the frequency. The parallel yellow curves in Figure 5b are therefore generated by the same moving aircraft. The four model parameters can be determined by the same technique used for the previous example event from the observed time and frequency data of two strong sources. This is illustrated in Figure 5c that shows the picked data (with outliers removed) and fitted curve of equations (1) and (3b). In this case, the flying velocity is 236 km/hr and the shortest distance between the flying object and the seismic station is 1260 m. Fitting separately the two sources with different central frequency f_0 gives same results. The obtained flying velocity, height, and existence of multiple central frequencies that may be produced by different rotor blades indicate that the source generating this type of data is a helicopter. Similar seismic records associated with helicopters flying over the Hekla Volcano in Iceland were discussed by Eibl et al. (2015). As the sensors used in this study have higher Nyquist frequency (250 Hz) than the ones used by Eibl et al. (2015; 50 Hz), our records cover a broader frequency range and contain many more overtones from 50 Hz to 220 Hz (Figure 5b).

To confirm that the source generating data of the type shown in Figures 4 and 5 is indeed a helicopter, we analyze seismic waveforms (Figure 7a) associated with a known helicopter event during maintenance of seismic stations at the Jackass Flat site on the SJFZ. Field notes indicate that the helicopter flew over

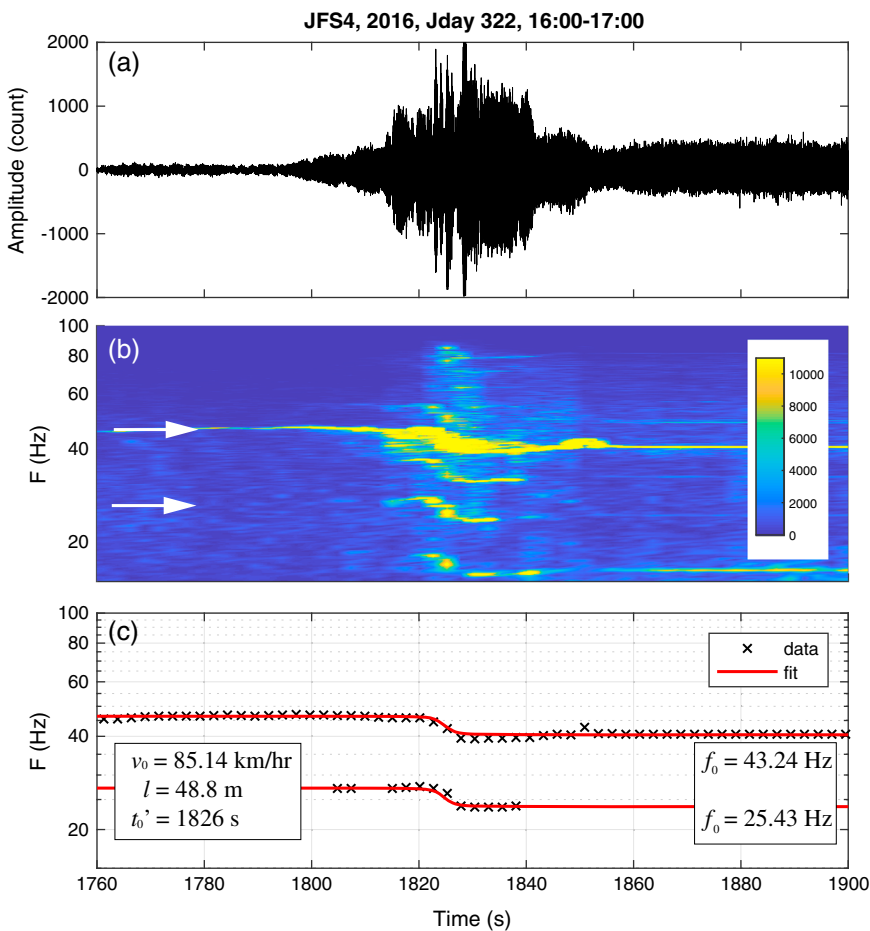


Figure 7. (a) A raw vertical component waveform for a known helicopter event flying over seismic station JFS4. (b) A corresponding spectrogram with vertical axis in log scale. The arrows denote the two strong overtones picked for analysis. (c) Time and frequency data (black crosses) for two overtones picked in the spectrogram in (b) and line fit to the data based on equation (1) (red curves). The inferred parameters for the helicopter are indicated in the box.

station JFS4 (red triangle in Figure 1a), slowed down, hovered, picked up a seismic sensor package, and then flew away from the site. Figure 7a shows a 140-s long raw waveform of a vertical component sensor associated with the helicopter flying over the site. The corresponding spectrogram is plotted with log scale for the frequency in Figure 7b. The results are very similar to those in Figures 4 and 5, showing clearly source signatures with multi f_0 values. Fitting frequency and time data of two f_0 sources indicates a flying velocity of ~85 km/hr and distance of ~50 m (Figure 7c). Since the helicopter was very close to the sensor and did not fly with constant velocity along a straight path, the data fits in this case are not as good as in Figure 5c.

To document the rate of occurrence and duration of air traffic events in the study area, we examine manually the entire data of the dense deployment and detect 892 airplane and helicopter events from Julian day 129 to 157 in 2014. Most events have a single f_0 source of the type shown in Figure 3 corresponding to airplanes, and 51 events have clear multiple f_0 sources of the type shown in Figures 5 and 8 characteristics of a helicopter source. The events identified as airplanes usually contain only one overtone (or sometime two) with frequencies above 70 Hz, and based on the Doppler analysis parameters, they have flying velocities higher than 300 km/hr. The events identified as helicopters contain many overtones covering frequencies above 15 Hz and have flying velocities below 250 km/hr.

Figure 8a displays a histogram of the number of detected air traffic events for each hour of the day. As expected, there are considerably more events during the daytime and very few events from 23:00 to 04:00 local time. The air traffic events have an average duration of ~200 s, so together they cover >7% of the

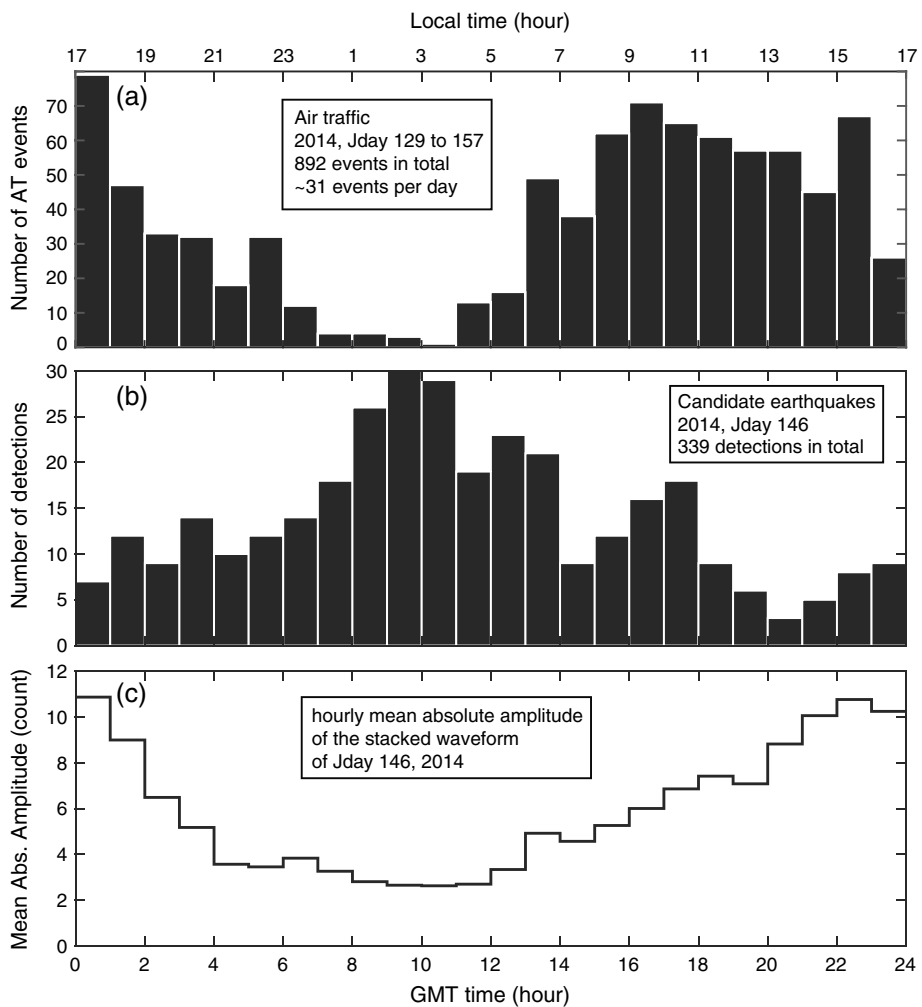


Figure 8. (a) A histogram of all detected air traffic events from Julian day 129 to 157, 2014, with about 31 air traffic events per day and relatively quiet time during the local night. (b) A histogram of high quality small candidate earthquakes detected Julian day 146 by Meng and Ben-Zion (2018). (c) Hourly mean absolute amplitude of stacked waveforms of the entire dense array in Julian day 146, 2014.

day. The total duration of such signals at locations with higher air traffic can cover a larger portion of the day. The detectability of small earthquakes is highly affected by the background noise level. Figure 8b shows a histogram of candidate small events detected in the dense deployment data during Julian day 146, 2014, with a technique involving several steps of stacking of subarrays and analyses of the stacked records with detector functions and beamforming (Meng & Ben-Zion, 2018). There are considerably more detections from 23:00 to 04:00 local time when the rate of air traffic events is low. The variation of the seismic noise during Julian day 146 is estimated by the hourly mean absolute amplitudes of stacked waveforms across the array (Figure 8c). The anticorrelation of the results with those of Figure 8a indicates that the air traffic events contribute significantly to the daily variations of the local noise level. The air traffic events can affect especially the detectability of very small earthquakes with high corner frequencies (e.g., $M \leq 1$) that are the target of recent detection efforts (e.g., Inbal et al., 2016; Li et al., 2018; Yoon et al., 2015). Other human activities producing noise over lower frequency bands can affect similarly the detectability of larger seismic events.

3. Discussion and Conclusions

We observe frequent daily airplane and helicopter events in continuous waveforms recorded by a dense seismic array at the SGB site on the SJFZ southeast of Anza, California (Figure 1a). Each event lasts several

minutes and resembles in seismograms tremor or collection of small earthquakes (e.g., Figures 2a and 3a). However, time-frequency analysis reveals clear Doppler effects that can be fitted well with a basic analytical solution in terms of flying velocity, average distance, and central frequency (equations (1) and (3b)). Airplane events have a simple signature involving typically a single central frequency (Figure 3b). They generate mainly frequencies higher than 70 Hz that can be removed from the data by low-pass filtering. Helicopter events are associated with several central frequencies and produce more complex signatures (Figures 5b and 7b) covering a broad frequency band and, hence, harder to remove from data. The air traffic events increase significantly the local noise level and reduce the detectability of small earthquakes (Figure 8). They should not affect typical noise-based imaging studies that use frequencies lower than 1 Hz but can affect noise-based applications with dense arrays and frequencies higher than 15 Hz (e.g., Figure 9 of Ben-Zion et al., 2015).

The acoustic wavelengths of typical air traffic events (<5 m with velocity of 343 m/s and frequency > 70 Hz) are shorter than the interstation spacing (~10–30 m), so beamforming cannot be used to determine the sources trajectories. However, the flying traces of airplanes can be determined by the technique described in Appendix A. The detectable distance of air traffic events can be found from the simple expression $\sqrt{l^2 + (v_0 t_d/2)^2}$, where t_d is the duration of the air traffic signal. The detectable distance is related to the strength of the waves radiated from the source and the background noise level. As examples, using $t_d \sim 150$ s for the airplane event in Figure 3 and $t_d \sim 220$ s for the helicopter event in Figure 5, the corresponding distances are ~9.0 km and ~7.3 km, respectively. Most detectable distances for other air traffic events are in the range 6–10 km.

Most airplane events have a single source f_0 , but some have two overtones as shown in the white dashed box in Figure 4b. The second source with higher f_0 is truncated by the corner frequency of sensor sensitivity at ~220 Hz. Both airplanes and helicopters may generate overtones with frequencies >250 Hz that are not recorded by the sensors. The radiation sources from airplane events are primarily the engines, perhaps augmented by additional weaker vibrations associated with the aircraft body and propellers (for small airplanes). The radiation sources from helicopters are more complex and are related to the engines and rotating propellers. More than 10 overtones of the helicopter event in Figure 5b demonstrate the possible multiple resonances produced by helicopters. Various conditions can distort the basic Doppler characteristics incorporated in the simple equations (1)–(3a) and (3b) and produce complex features of the type shown in right white dashed box in Figure 2b. These include significant changes in the aircraft speed, flying direction, interaction of small aircraft with strong wind gusts, etc. Figures S2 to S4 provide additional examples of complex signals produced by air traffic events.

In the relatively remote location of the study area there are several air traffic events per hour, except during local nighttime (Figure 8a), producing together ground motion over 7% of the day. In locations closer to airports and large cities (e.g., Long Beach, Los Angeles) the air traffic events can cover a significantly larger portion of the day. As example, the Los Angeles International airport handled in 2016 on average 1,910 aircraft landings and takeoffs per day (http://www.lawa.org/welcome_lax.aspx?id=40). Assuming that each event lasts about ~200 s, and that the events have 75% overlap, signals generated by airplanes (and helicopters) exist in the entire portion of the day (e.g., 16–18 hr) with significant air traffic activity. The ground vibration generated by air traffic events can mask and prevent detection of signals associated with very small seismic sources (Figure 8b), or in worse cases misidentified as small earthquakes or tremor (e.g., Eibl et al., 2015). To highlight the importance of the results for current efforts to detect small earthquakes, we estimate below the expected duration of ground motion generated in a day by small local earthquakes.

The total duration T of daily earthquakes in the magnitude range $M_1 \leq M \leq M_2$ is given by the integral

$$T = \int_{M_1}^{M_2} \tau(M) \cdot n(M) dM, \quad (6)$$

where $\tau(M)$ is the duration of an earthquake with magnitude M and n is the number of events around magnitude M given by the Gutenberg-Richter relation

$$\log(n) = a - bM. \quad (7)$$

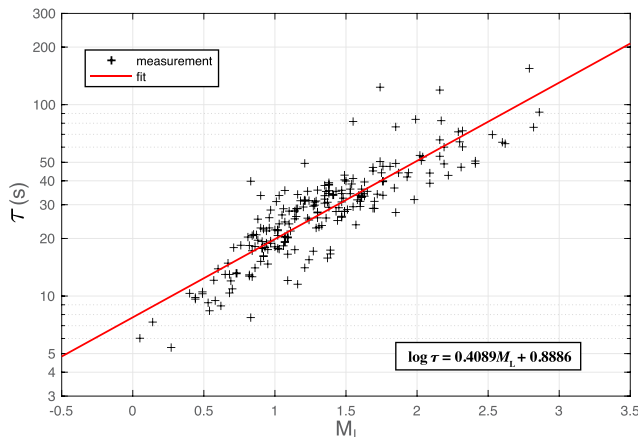


Figure 9. Measured durations of earthquakes with different local magnitudes (black crosses) and a fitted line (red) associated with the scaling relation indicated in the box.

The b value of the Gutenberg-Richter relation is typically around 1, while the a value depends strongly on the location and time (e.g., Zaliapin & Ben-Zion, 2013, 2016). To evaluate the expected daily earthquake duration for the study area, we use the technique illustrated in Appendix B to measure the duration of 266 cataloged earthquakes (Hauksson et al., 2012) in the magnitude range $0 \leq M \leq 3$ recorded by three-component station SGBF0 (Figure 9). The results can be summarized by the scaling relation

$$\log \tau(M) = 0.41M + 0.89. \quad (8)$$

Using $\log \tau$ in the scaling relation avoids getting negative duration for earthquakes with small magnitudes. Combining equations (6)–(8), we get

$$T = \int_{M_1}^{M_2} 10^{0.41M+0.89} \cdot 10^{a-bM} dM. \quad (9)$$

To evaluate (9) for daily seismicity in the trifurcation area of the SJFZ, we use $b = 1$ and $a = 1.5/\text{day}$. Integrating with these constants equation (9) over the magnitude range $0 \leq M \leq 3$ gives total daily earthquake duration of 178 s, which covers 0.2% of the day. Reducing M_1 to -1 and -2 , and assuming the scaling relation of equation (8) can be extrapolated to lower magnitude than those used in Figure 9, increases the estimated total duration covered by earthquakes to 0.8% and 3.2% of the day, respectively. Reducing further the lower magnitude limit to -4.54 gives a total duration of a full day. These total earthquake duration estimates are gross upper bounds, since many small regional events may overlap in time and many small events not sufficiently close to the recording site will not produce observable signals (e.g., Kwiatek & Ben-Zion, 2016). Increasing the upper magnitude limit to 5 has negligible affect on the results because the rate of higher magnitude events is very low. We note that the seismicity rate, and hence the a value, in the trifurcation area is the highest in southern California (Ross et al., 2017), so corresponding estimates of earthquake durations in most other regions will be smaller than those given above.

The results of this study demonstrate that seismic arrays can be used to detect and quantify flight parameters of aircrafts (these should include low flying and stealth airplanes that evade radar detection). The presented results contribute to the growing recognition of different types of surface and atmospheric events (e.g., car traffic, trains, storms, wind turbines, and air traffic) producing signals that are contained in observed seismograms (e.g., Eibl et al., 2015; Fuchs & Bokelmann, 2017; Neuffer & Kremers, 2017; Salvermoser et al., 2015; Tanimoto & Valovcin, 2015). In the study area near Anza California, the total duration of air traffic signals ($> 7\%$ of the day) is likely larger than the duration covered by earthquake signals. In many other places, and especially large urban areas with highly active airports, the duration of air traffic signals can exceed 50% of the day and be significantly larger than the duration of seismic events. Continuing efforts to recognize characteristic signatures of various anthropogenic and atmospheric sources of ground motion, and separating these sources from weak subsurface earthquakes and tremor, will help develop refined catalogs of seismic sources and improved understanding of the observed seismic wavefield.

Appendix A: Finding the Flying Traces of Airplanes

To model the flying trace of an aircraft, we consider a reference point $\vec{r} = [x \ 0 \ z]$ on the trace and a direction vector $\hat{e} = [e_x \ e_y \ e_z]$ with $e_x^2 + e_y^2 + e_z^2 = 1$. The reference times t_0' for all stations gives good constraint for the direction vector. Figure A1 displays the geometry of the flying trace and two example stations. At time $t' = t_{01}'$, station S_1 receives the signal of the aircraft radiated at time t_1 at point A_1 . From equation (3b), when $t' = t_{01}'$, $t = -l_1/\sqrt{c^2 - v_0^2}$. This means it takes the acoustic wave $l_1/\sqrt{c^2 - v_0^2}$ to propagate from A_1 to S_1 . Therefore, the length of line segment $|A_1S_1| = cl_1/\sqrt{c^2 - v_0^2}$, the length of line segment $|A_1B_1| = v_0 l_1/\sqrt{c^2 - v_0^2}$, and

$$t_{01}' = t_1 + \frac{|A_1S_1|}{c} = t_1 + \frac{l_1}{\sqrt{c^2 - v_0^2}}. \quad (\text{A1})$$

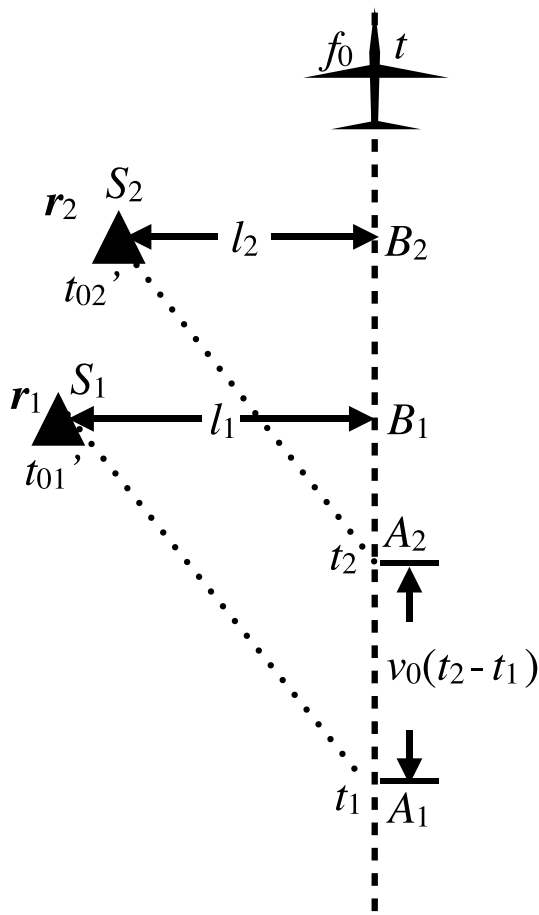


Figure A1. A conceptual diagram of an aircraft flying over two example stations.

By performing similar estimates for station S_2 , the length of line segment $|A_2B_2| = v_0l_2/\sqrt{c^2 - v_0^2}$, the length of line segment $|A_2S_2| = cl_2/\sqrt{c^2 - v_0^2}$, and

$$t_{02}' = t_2 + \frac{|A_2S_2|}{c} = t_2 + \frac{l_2}{\sqrt{c^2 - v_0^2}}. \quad (\text{A2})$$

Subtracting equation (A1) from (A2),

$$t_{02}' - t_{01}' = t_2 - t_1 + \frac{l_2 - l_1}{\sqrt{c^2 - v_0^2}}. \quad (\text{A3})$$

The location of station S_1 is \vec{r}_1 , the location of station S_2 is \vec{r}_2 , and the length of $|B_1B_2| = \hat{e} \cdot (\vec{r}_2 - \vec{r}_1)$. Based on simple geometrical consideration,

$$\begin{aligned} |A_1A_2| &= |A_1B_1| + |B_1B_2| - |A_2B_2| \\ &= \frac{v_0l_1}{\sqrt{c^2 - v_0^2}} + \hat{e} \cdot (\vec{r}_2 - \vec{r}_1) - \frac{v_0l_2}{\sqrt{c^2 - v_0^2}}. \end{aligned} \quad (\text{A4})$$

Substituting $t_2 - t_1$ in equation (A3) with $|A_1S_1|/v_0$,

$$t_{02}' - t_{01}' = \frac{\hat{e} \cdot (\vec{r}_2 - \vec{r}_1)}{v_0}, \quad (\text{A5})$$

where the reference times (t_{01}' and t_{02}') are given by the data and equations (4a) and (4b), and v_0 is determined by the mean of the observed flying velocity for all stations. By picking a reference station, we can build a matrix for inversion of the direction vector. Among the three components of the direction vector, only two are independent. Using the constraint $e_x^2 + e_y^2 + e_z^2 = 1$ and equations (4a) and (4b), the inversion for the direction vector \hat{e} converges quickly within a couple of iterations.

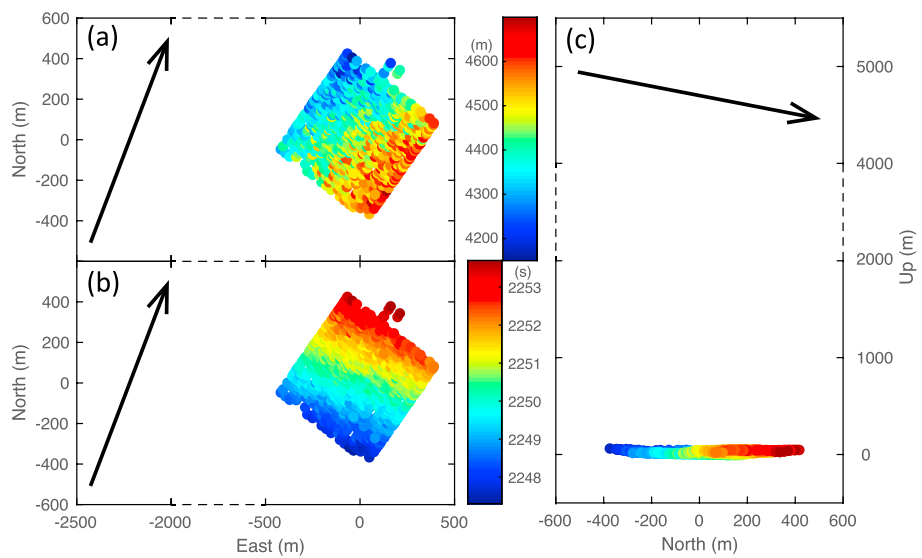


Figure A2. (a) Distribution of the distance l (colored circles) based on data at all stations for the example event 1 in Figure 3. (b) Corresponding t' distribution. (c) A northward cross section showing the height of the flying trace. The black arrows mark the inferred flying trace of the airplane.

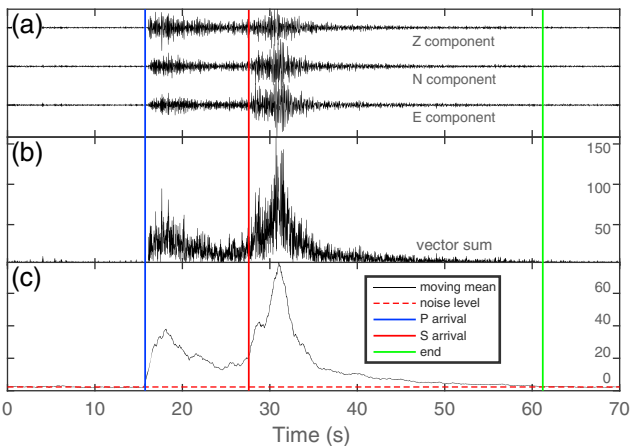


Figure B1. An illustration of estimating duration for example event with M_L 2.41 and epicenter distance of 95 km recorded by a three-component station SGBF0. (a) Z, N, and E component waveforms band-pass filtered between 2 and 15 Hz. (b) The vector sum of the three-component waveforms. (c) The moving mean of the vector sum. The red dashed horizontal line denotes the noise level, while the blue, red, and green vertical lines show the P and S arrivals and the end of the coda.

ograms at 2–15 Hz to increase the SNR. Figures B1a and B1b show, respectively, the filtered three-component waveforms and vector sum of the three components for this event. A 1-D model obtained by averaging the 3-D velocity model of Lee et al. (2014) for the southern California region shown in Figure 1a is used to calculate predicted P and S arrivals (vertical blue and red lines). To estimate the end time of the coda waves, we calculate a moving mean of the vector sum to get a smooth envelop of the waveform (Figure B1c). Since the earthquake durations can have several orders of time intervals, we use for each event a moving window length that depends on the source duration.

The source duration is estimated as follows. We first estimate the rupture size of each event, assuming it is approximately a circular crack with radius r sustaining a uniform strain drop $\Delta\epsilon$ in a Poissonian solid. The seismic potency (moment/rigidity) in this case (appropriate for the analyzed small events) is given by (Ben-Zion, 2008; Eshelby, 1957)

$$P_0 = \frac{16}{7} \Delta\epsilon r^3. \quad (\text{B1})$$

The seismic potency and magnitude of earthquakes spanning a relatively small range of magnitudes are related empirically by a relation of the type (e.g., Ben-Zion & Zhu, 2002; Hanks & Kanamori, 1979)

$$\log P_0 = d \cdot M + e. \quad (\text{B2})$$

For small earthquakes in southern California, $d = 1$ and $e = -4.7$ with potency units in square kilometers per centimeter (Ben-Zion & Zhu, 2002). Combining equations (B1) and (B2) and assuming an average strain drop $\Delta\epsilon = 10^{-4}$, the radius in unit of kilometers of an earthquake with magnitude M is

$$r(M) = \left[\frac{10^{-1}}{(16/7)} \right] \cdot 10^{\frac{(dM+e)}{3}}, \quad (\text{B3})$$

where the 10^{-1} factor stems from using $\Delta\epsilon = 10^{-4}$ and including a unit conversion of P_0 from square kilometers times centimeter to cubic kilometers. Assuming an average rupture propagation velocity of $0.9V_S$, with shear wave velocity $V_S \approx 3$ km/s, the source duration for an earthquake with magnitude M is

$$T_{sd} = \frac{r(M)}{0.9V_S} = 0.0162 \cdot 10^{\frac{(dM+e)}{3}}. \quad (\text{B4})$$

In the performed analysis we use $500 \cdot T_{sd}$ as the length of the time window to calculate the moving mean of the vector sum (Figure B1c). Using somewhat smaller and larger window length gives essentially the same

There are only two independent parameters for the reference point \vec{r} of the flying trace. By fitting the data with Doppler effect, the distance between each station and the flying trace is displayed as the colored circles in Figure A2a. From the Pythagoras theorem, the distance is

$$l = \sqrt{(\vec{r} - \vec{r}_{st})^2 - [(\vec{r} - \vec{r}_{st}) \cdot \hat{e}]^2}. \quad (\text{A6})$$

By using the same inversion technique equations (4a) and (4b), \vec{r} can be determined by the direction vector \hat{e} , station location \vec{r}_{st} , and the observed distances. The flying trace of the example event in Figure 3 is marked by black arrows in Figure A2. This flight trace moves to the northeast with a height of about 4.5 km.

Appendix B: Estimating Earthquake Durations

The durations of earthquakes depend on site conditions. To estimate a basic scaling relation $\tau(M)$ at the SGB site on the San Jacinto fault zone, we measure the durations of 266 earthquakes from the catalog of Hauksson et al. (2012) recorded by the strong ground motion station SGBF0 (Figure 1c) from Julian day 129 to 157, 2014. The procedure is illustrated in Figure B1 for an M_L 2.41 earthquake with epicentral distance of 95 km. For each event we first band-pass filter the acceler-

ograms at 2–15 Hz to increase the SNR. Figures B1a and B1b show, respectively, the filtered three-component waveforms and vector sum of the three components for this event. A 1-D model obtained by averaging the 3-D velocity model of Lee et al. (2014) for the southern California region shown in Figure 1a is used to calculate predicted P and S arrivals (vertical blue and red lines). To estimate the end time of the coda waves, we calculate a moving mean of the vector sum to get a smooth envelop of the waveform (Figure B1c). Since the earthquake durations can have several orders of time intervals, we use for each event a moving window length that depends on the source duration.

The source duration is estimated as follows. We first estimate the rupture size of each event, assuming it is approximately a circular crack with radius r sustaining a uniform strain drop $\Delta\epsilon$ in a Poissonian solid. The seismic potency (moment/rigidity) in this case (appropriate for the analyzed small events) is given by (Ben-Zion, 2008; Eshelby, 1957)

$$P_0 = \frac{16}{7} \Delta\epsilon r^3. \quad (\text{B1})$$

The seismic potency and magnitude of earthquakes spanning a relatively small range of magnitudes are related empirically by a relation of the type (e.g., Ben-Zion & Zhu, 2002; Hanks & Kanamori, 1979)

$$\log P_0 = d \cdot M + e. \quad (\text{B2})$$

For small earthquakes in southern California, $d = 1$ and $e = -4.7$ with potency units in square kilometers per centimeter (Ben-Zion & Zhu, 2002). Combining equations (B1) and (B2) and assuming an average strain drop $\Delta\epsilon = 10^{-4}$, the radius in unit of kilometers of an earthquake with magnitude M is

$$r(M) = \left[\frac{10^{-1}}{(16/7)} \right] \cdot 10^{\frac{(dM+e)}{3}}, \quad (\text{B3})$$

where the 10^{-1} factor stems from using $\Delta\epsilon = 10^{-4}$ and including a unit conversion of P_0 from square kilometers times centimeter to cubic kilometers. Assuming an average rupture propagation velocity of $0.9V_S$, with shear wave velocity $V_S \approx 3$ km/s, the source duration for an earthquake with magnitude M is

$$T_{sd} = \frac{r(M)}{0.9V_S} = 0.0162 \cdot 10^{\frac{(dM+e)}{3}}. \quad (\text{B4})$$

results. The noise level is estimated as the root-mean-square of a 10-s moving mean window before the *P* arrival (red horizontal dashed line in Figure B1c). The end of the coda waves is picked when the moving mean drops to noise level (vertical green line). The duration of each analyzed earthquake is estimated as the time between the *P* arrival and the end of the coda waves.

Acknowledgments

The seismic data used in this paper can be obtained from the Data Management Center of the Incorporated Research Institutions for Seismology and Broadband Seismic Data Collection Center (Vernon et al., 2014; Vernon & Ben-Zion, 2010). The manuscript benefitted from constructive comments by Florian Fuchs and an anonymous referee. The study was supported by the National Science Foundation (grant EAR-1551411) and the Department of Energy (award DE-SC0016520).

References

- Bensen, G. D., Ritzwoller, M. H., Barmin, M. P., Levshin, A. L., Lin, F., Moschetti, M. P., et al. (2007). Processing seismic ambient noise data to obtain reliable broad-band surface wave dispersion measurements. *Geophysical Journal International*, 169(3), 1239–1260. <https://doi.org/10.1111/j.1365-246X.2007.03374.x>
- Ben-Zion, Y. (2008). Collective behavior of earthquakes and faults: Continuum-discrete transitions, evolutionary changes and corresponding dynamic regimes. *Reviews of Geophysics*, 46, RG4006. <https://doi.org/10.1029/2008RG000260>
- Ben-Zion, Y., Vernon, F. L., Ozakin, Y., Zogone, D., Ross, Z. E., Meng, H. R., et al. (2015). Basic data features and results from a spatially dense seismic array on the San Jacinto fault zone. *Geophysical Journal International*, 202(1), 370–380. <https://doi.org/10.1093/gji/ggv144>
- Ben-Zion, Y., & Zhu, L. (2002). Potency-magnitude scaling relations for southern California earthquakes with $1.0 < M_L < 7.0$. *Geophysical Journal International*, 148(3), F1–F5. <https://doi.org/10.1046/j.1365-246X.2002.01637.x>
- Campillo, M., Roux, P., & Shapiro, N. M. (2011). Seismic, Ambient Noise Correlation. In H. K. Gupta (Ed.), *Encyclopedia of Solid Earth Geophysics* (pp. 1230–1236). Dordrecht, Netherlands: Springer. https://doi.org/10.1007/978-90-481-8702-7_218
- Chen, X., Nakata, N., Pennington, C., Haffner, J., Chang, J. C., He, X., et al. (2017). The Pawnee earthquake as a result of the interplay among injection, faults and foreshocks. *Scientific Reports*, 7(1), 4945. <https://doi.org/10.1038/s41598-017-04992-z>
- Eibl, E. P., Lokmer, I., Bean, C. J., Akerlie, E., & Vogfjörd, K. S. (2015). Helicopter vs. volcanic tremor: Characteristic features of seismic harmonic tremor on volcanoes. *Journal of Volcanology and Geothermal Research*, 304, 108–117. <https://doi.org/10.1016/j.jvolgeores.2015.08.002>
- Eshelby, J. D. (1957). The determination of the elastic field of an ellipsoidal inclusion and related problems. *Proceedings of the Royal Society of London Series A*, 241(1226), 376–396. <https://doi.org/10.1098/rspa.1957.0133>
- Fuchs, F., & Bokelmann, G. (2017). Equidistant spectral lines in train vibrations. *Seismological Research Letters*, 89(1), 56–66. <https://doi.org/10.1785/0220170092>
- Gradon, C., Roux, P., Moreau, L., & Ben-Zion, Y. (2017). Detecting and locating surface and shallow seismic sources using a dense array of sensors on the San Jacinto fault, Abstract for the fall AGU meeting.
- Hanks, T. C., & Kanamori, H. (1979). A Moment Magnitude Scale. *Journal of Geophysical Research*, 84(B5), 2348–2350. <https://doi.org/10.1029/JB084iB05p02348>
- Hauksson, E., Yang, W., & Shearer, P. M. (2012). Waveform relocated earthquake catalog for Southern California (1981 to June 2011). *Bulletin of the Seismological Society of America*, 102(5), 2239–2244. <https://doi.org/10.1785/0120120010>
- Hillers, G., Roux, P., Campillo, M., & Ben-Zion, Y. (2016). Focal spot imaging based on zero lag cross correlation amplitude fields: Application to dense array data at the San Jacinto fault zone. *Journal of Geophysical Research: Solid Earth*, 121, 8048–8067. <https://doi.org/10.1002/2016JB013014>
- Inbal, A., Ampuero, J. P., & Clayton, R. W. (2016). Localized seismic deformation in the upper mantle revealed by dense seismic arrays. *Science*, 354(6308), 88–92. <https://doi.org/10.1126/science.aaf1370>
- Kwiatek, G., & Ben-Zion, Y. (2016). Theoretical limits on detection and analysis of small earthquakes. *Journal of Geophysical Research: Solid Earth*, 121, 5898–5916. <https://doi.org/10.1002/2016JB012908>
- Lee, E. J., Chen, P., Jordan, T. H., Maechling, P. B., Denolle, M. A., & Beroza, G. C. (2014). Full-3-D tomography for crustal structure in southern California based on the scattering-integral and the adjoint-wavefield methods. *Journal of Geophysical Research: Solid Earth*, 119, 6421–6451. <https://doi.org/10.1002/2014JB011346>
- Li, Z., Peng, Z., Hollis, D., Zhu, L., & McClellan, J. (2018). High-resolution seismic event detection using local coherence for large-N arrays. *Scientific Reports*, 8(1), 1646. <https://doi.org/10.1038/s41598-018-19728-w>
- Meng, H., & Ben-Zion, Y. (2018). Detection of small earthquakes with dense array data: Example from the San Jacinto fault zone, southern California. *Geophysical Journal International*, 212(1), 442–457. <https://doi.org/10.1093/gji/ggx404>
- Nakata, N., Chang, J. P., Lawrence, J. F., & Boué, P. (2015). Body wave extraction and tomography at Long Beach, California, with ambient-noise interferometry. *Journal of Geophysical Research: Solid Earth*, 120, 1159–1173. <https://doi.org/10.1002/2015JB011870>
- Neuffer, T., & Kremers, S. (2017). How wind turbines affect the performance of seismic monitoring stations and networks. *Geophysical Journal International*, 211(3), 1319–1327. <https://doi.org/10.1093/gji/ggx370>
- Ross, Z. E., Hauksson, E., & Ben-Zion, Y. (2017). Abundant off-fault seismicity and orthogonal structures in the San Jacinto fault zone. *Science Advances*, 3(3), e1601946. <https://doi.org/10.1126/sciadv.1601946>
- Roux, P., Moreau, L., Lecointre, A., Hillers, G., Campillo, M., Ben-Zion, Y., et al. (2016). A methodological approach toward high-resolution surface wave imaging of the San Jacinto Fault Zone using ambient-noise recordings at a spatially dense array. *Geophysical Journal International*, 206(2), 980–992. <https://doi.org/10.1093/gji/ggw193>
- Salvermoser, J., Hadzioannou, C., & Stähler, S. (2015). Structural monitoring of a highway bridge using passive noise recordings from street traffic. *The Journal of the Acoustical Society of America*, 138(6), 3864–3872. <https://doi.org/10.1121/1.4937765>
- Shapiro, N. M., Campillo, M., Margerin, L., Singh, S. K., Kostoglou, V., & Pacheco, J. (2000). The energy partitioning and the diffusive character of the seismic coda. *Bulletin of the Seismological Society of America*, 90(3), 655–665. <https://doi.org/10.1785/0119990021>
- Shelly, D. R., Beroza, G. C., & Ide, S. (2007). Non-volcanic tremor and low-frequency earthquake swarms. *Nature*, 446(7133), 305–307. <https://doi.org/10.1038/nature05666>
- Tanimoto, T., & Valovcin, A. (2015). Stochastic excitation of seismic waves by a hurricane. *Journal of Geophysical Research: Solid Earth*, 120, 7713–7728. <https://doi.org/10.1002/2015JB012177>
- Vernon, F., & Ben-Zion, Y. (2010). San Jacinto Fault Zone experiment. International Federation of Digital Seismograph Networks. Other/Seismic Network. https://doi.org/10.7914/SN/YN_2010
- Vernon, F., Ben-Zion, Y., & Hollis, D. (2014). Sage Brush Flats Nodal Experiment. International Federation of Digital Seismograph Networks. Other/Seismic Network. https://doi.org/10.7914/SN/ZG_2014
- Weaver, R. L. (1982). On diffuse waves in solid media. *The Journal of the Acoustical Society of America*, 71(6), 1608–1609. <https://doi.org/10.1121/1.387816>

- Yoon, C. E., O'Reilly, O., Bergen, K. J., & Beroza, G. C. (2015). Earthquake detection through computationally efficient similarity search. *Science Advances*, 1(11), e1501057. <https://doi.org/10.1126/sciadv.1501057>
- Zaliapin, I., & Ben-Zion, Y. (2013). Earthquake clusters in southern California I: Identification and stability. *Journal of Geophysical Research: Solid Earth*, 118, 2847–2864. <https://doi.org/10.1002/jgrb.50179>
- Zaliapin, I., & Ben-Zion, Y. (2016). A global classification and characterization of earthquake clusters. *Geophysical Journal International*, 207(1), 608–634. <https://doi.org/10.1093/gji/ggw300>
- Zigone, D., Rivet, D., Radiguet, M., Campillo, M., Voisin, C., Cotte, N., et al. (2012). Triggering of tremors and slow slip event in Guerrero, Mexico, by the 2010 M_w 8.8 Maule, Chile, earthquake. *Journal of Geophysical Research*, 117, B09304. <https://doi.org/10.1029/2012JB009160>